15 Sep 2022

Atomic Layer Deposited Pt/TiO2-SiO2 and Pt/ZrO2-SiO2 for Sequential Adsorption and Oxidation of VOCs

Busuyi O. Adebayo

Han Yu

Ali A. Rownaghi
Missouri University of Science and Technology, rownaghia@mst.edu

Xinhua Liang
Missouri University of Science and Technology, liangxin@mst.edu

et. al. For a complete list of authors, see https://scholarsmine.mst.edu/che_bioeng_facwork/1030

Recommended Citation

B. O. Adebayo et al., "Atomic Layer Deposited Pt/TiO2-SiO2 and Pt/ZrO2-SiO2 for Sequential Adsorption and Oxidation of VOCs," *Chemical Engineering Journal*, vol. 444, article no. 136603, Elsevier, Sep 2022.
The definitive version is available at https://doi.org/10.1016/j.cej.2022.136603

Chemical Engineering Journal 444 (2022) 136603

Contents lists available at ScienceDirect

Chemical Engineering Journal

journal homepage: www.elsevier.com/locate/cej

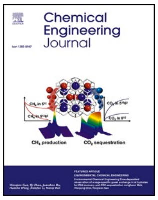

Atomic layer deposited Pt/TiO_2-SiO_2 and Pt/ZrO_2-SiO_2 for sequential adsorption and oxidation of VOCs

Busuyi O. Adebayo, Han Yu, Ali A. Rownaghi, Xinhua Liang, Fateme Rezaei *

Department of Chemical & Biochemical Engineering, Missouri University of Science and Technology, 1101 N State Street, Rolla, MO 65409, United States

ARTICLE INFO

Keywords:
VOC
Adsorption
Oxidation
Catalysis
Mixed-metal oxide
Pt
ALD

ABSTRACT

In this work, Pt nanoparticles were loaded on SiO_2, TiO_2-thin-film-modified SiO_2 (TiO_2-SiO_2), or ZrO_2-thin-film-modified SiO_2 (ZrO_2-SiO_2) particles and the composites were investigated for sequential adsorption and desorption/catalytic oxidation of benzene. The SiO_2 was prepared via sol–gel method, while TiO_2-SiO_2 and ZrO_2-SiO_2 were synthesized via atomic layer deposition (ALD) thin film coating of TiO_2 or ZrO_2 on SiO_2 particles substrate. In the sequential capture-reaction tests, the materials were first exposed to ca. 500 ppm_v benzene gas at 25 °C and 1 atm until 5% breakthrough was attained, followed by tandem desorption and catalytic oxidation while raising bed temperature to 200 °C. The benzene vapor adsorption isotherms followed type-IV isotherm classification, revealing a combination of monolayer, multilayer and capillary condensation adsorption mechanisms in sequence. The xPt/ZrO_2-SiO_2 materials exhibited superior capture-conversion capabilities relative to their xPt/TiO_2-SiO_2. In particular, 3Pt/ZrO_2-SiO_2, prepared with 3 cycles of Pt ALD, exhibited the maximum *in-situ* conversion at ~ 100% and turnover frequency of 17.1 $mmol_{C6H6}/mol_{Pt}/s$ with a dynamic adsorption capacity of 0.45 mmol/g, indicating synergistic effects of Pt nanoparticles and ZrO_2 in the ALD-based dual-function materials.

1. Introduction

One of the largest emissions of volatile organic compounds (VOCs) is found in a group of aromatic hydrocarbons comprising benzene, toluene/methylbenzene, ethylbenzene and xylene/trimethylbenzene (BTEX) [1]. The removal of these compounds from air or process streams has been accomplished by adsorption, thermal or catalytic oxidation, and less commonly by biofiltration and absorption [2,3]. Despite substantial advancements in VOC abatement methods, they continue to have serious flaws. Adsorption, for example, has been shown to be effective in the removal of VOCs from dilute to ultra-dilute streams, but its efficacy degrades in humid conditions. Thermal oxidation is effective in handling concentrated streams of VOCs and all VOCs burn, unfortunately it requires a large amount of energy and even more for dilute streams making it less efficient. On the other hand, the catalytic oxidation that has been used to address the drawback of thermal oxidation often requires a large amount of catalyst inventory, which is paired with catalyst deactivation commonly via aging/sintering, fouling/coking, and poisoning. As a result, there is still room for advancement in such systems, particularly for handling dilute to ultra-dilute VOC streams. Concentrating ppm-level VOCs in-situ, before their oxidation, offers a practical approach to reduce the catalyst inventory and capital cost associated with VOC emissions abatement.

Currently, integrated approaches such as adsorptive reactors, are being investigated to address the challenges of the conventional VOC abatement techniques. Adsorptive reactors allow for process intensification while reducing capital investment, catalyst inventories, and the need for external energy or cooling capacity. The combined adsorption-catalysis strategy involves first concentrating the adsorbate through adsorption, followed by combustion, in which the adsorbed VOCs are transformed in-situ to H_2O and CO_2. For example, Kullavanijaya et al. [4] in their work employed an integrated technique to concentrate a VOC-lean stream over a solid adsorbent in a low-temperature adsorption bed before being combusted directly or catalytically in an incinerator for conversion to innocuous chemicals. Same Kullavanijaya et al. [5] in their later work treated binary VOC mixtures by adsorption on activated carbon followed by catalytic oxidation on a CeO_2/Al_2O_3-supported palladium catalyst. Similarly, Nikolajsen et al. [6] evaluated the efficacy of a sintered-metal-fiber (SMF) supported adsorbent-catalyst in sequential adsorption and oxidation of a dilute VOC-laden air stream. In

---

* Corresponding author.
E-mail address: rezaeif@mst.edu (F. Rezaei).

https://doi.org/10.1016/j.cej.2022.136603
Received 1 March 2022; Received in revised form 9 April 2022; Accepted 22 April 2022
Available online 25 April 2022

a similar effort, Wang et al. [7] recently succeeded in removing bulky aromatics (toluene, o-xylene, and 1,3,5-trimethylbenzene) from bifunctional Ru/HZSM-5 via a hybrid adsorption-combustion approach. Furthermore, numerical modeling was used to investigate the application, practicality, and possible benefits of an adsorptive reactor for VOC abatement [8]. The right selection of materials for increased performance is one of the most important parts of the integrated approach.

Carbonaceous materials [9], metal oxides [10], zeolites [11], and metal–organic frameworks (MOFs)[12] have all been studied for adsorption of VOCs from industrial waste streams or contaminated air. As for the catalytic oxidation of VOCs, although noble metals (most notably Pd, Pt, Ru, Rh, Ir, Os, Ag, and Au) are the best materials due to their high activity, stability and selectivity [13], their high cost has prompted research into more cost-effective alternatives such as transition metal oxides (e.g., Ti, Zr, Al, Ni, Cu, Fe, and Zn) [14]. Lone transition metal oxides are however less active and less stable than the noble metals [15], prompting the development mixed-metal oxides (MMOs) whose synergistic effects considerably increase their catalytic activity. Moreover, supported noble metals perform better than bulk noble metals as catalysts on the basis of high dispersion of the metals on the support. Silica is commonly used as a support because it is cheap and has high interior surface area. Unfortunately, it has weak metal-support interaction which frequently leads to sintering/aging of the catalyst. Zirconia or titania has frequently been used to enhance the interaction between Pt and SiO_2 support which further enhances the dispersion and redox activity of Pt.

Atomic layer deposition (ALD) is a promising technique for MMOs coating. It is a surface-controlled layer-by-layer coating process based on self-limiting surface reactions and has been used to deposit nanostructure metal oxide films on supports. It is very suitable and efficient for this application [16]. Lee et al. [17], for example, found that ALD-coated TiO_2 thin films on a nano-structured Al_2O_3 membrane anode had a high toluene adsorption capacity and selectivity. Their results showed that about 277 mg/g of toluene can be captured via dynamic adsorption. Similarly, Liotta et al. [13] in their investigation used supported noble metals for hybrid adsorption-catalysis of VOCs. The authors attributed the improved performance of these materials to the synergetic effects of the doped heteroatom. Despite scientific substantiation of thin-film materials' potential as an adsorbent and/or catalyst for VOC abatement [18], there is little evidence of their application in the literature.

In our previous work [19], Ni nanoparticles were deposited on ZrO_2-SiO_2 via ALD method and the materials were investigated for sequential adsorption anddesorption/catalytic oxidation of benzene. The materials depicted good surface characteristics with excellent benzene adsorption performance. Benzene conversions of 85–95% and turnover frequencies (TOF) of 1.28–16.42 $\text{mmol}_{C6H6}/\text{mol}_{Ni}/s$ were reported over these materials. Aiming at developing novel dual-function materials (DFMs) with efficient adsorptive and catalytic performances, we embarked on a follow-up study to explore the concerted advantages offered by hybrid adsorption-catalysis and ALD methods. Specifically, in this study we incorporated a supposedly better catalyst, Pt nanoparticles into zirconia-silica and titania-silica supports (Pt/ZrO_2-SiO_2 and Pt/TiO_2-SiO_2, respectively) and, for comparison, on bare porous silica (Pt/SiO_2), via ALD with varied Pt loadings. The SiO_2 was synthesized by the sol–gel method while the mixed-metal oxide supports (ZrO_2-SiO_2 and TiO_2-SiO_2) were prepared by depositing ZrO_2 or TiO_2 thin films on the previously prepared porous SiO_2 particles by ALD. The materials were then tested for their adsorption capacities and thereafter evaluated for their sequential adsorption-catalytic performance to oxidize benzene to less benign compounds.

2. Experimental section

2.1. Materials

Tetraethyl orthosilicate (TEOS, 99%), hexadecyltrimethylammonium bromide (CTAB, 99%), tetrakis(dimethylamido) zirconium (IV) (TDMAZ, electronic grade, ≥ 99.99%), triethanolamine (TEAH, 98%), and tetrakis(dimethylamido)titanium (IV) (TDMAT, electronic grade, ≥ 99.99%) were purchased from Sigma-Aldrich, while (methylcyclopentadienyl)trimethyl platinum (IV) ((MeCp)$PtMe_3$, ≥ 98%) was purchased from Strem. Ultrahigh purity helium, hydrogen, nitrogen, and oxygen gases were purchased from Airgas. These chemicals and gases were used as purchased without further purification.

2.2. Materials synthesis

A detailed procedure for the synthesis of the UVM-7 silica support used in this work is reported in our previous work [10]. On this silica support, a supposedly ultra-thin ZrO_2 film was deposited via ALD. On top of the ZrO_2 film, well-dispersed Pt nanoparticles were deposited also via ALD. The details of the home-made fluidized bed reactor used for the ALD are described elsewhere [20]. The synthesized silica was outgassed at 200 °C for 3 h under vacuum before the ALD process. Thereafter, Pt/SiO_2 was prepared by depositing Pt nanoparticles on the outgassed silica using ALD. (MeCp)$PtMe_3$ was delivered into the reactor after it was heated to 100 °C. Typically, a cycle of Pt ALD consisted of a (MeCp)$PtMe_3$ dose, followed by an N_2 flush, which was followed by an H_2 dose and, finally, an N_2 flush. A temperature of 300 °C was maintained for the Pt ALD reaction. For the Pt/TiO_2-SiO_2 and Pt/ZrO_2-SiO_2 materials, TiO_2 or ZrO_2 film was first deposited on SiO_2 through 5 cycles of ALD and subsequently Pt ALD on the outgassed porous silica. A typical TiO_2 or ZrO_2 ALD cycle consisted of a TDMAT or TDMAZ dose, followed by an N_2 flush, which was followed by a deionized water dose and, finally, an N_2 flush. During the TiO_2 and ZrO_2 ALD, a temperature of 200 °C was maintained, and TDMAT or TDMAZ was delivered into the reactor after it has been heated to 80 °C. The samples were named *x*Pt/Si (group-1 materials), *x*Pt/TiSi (group-2 materials) and *x*Pt/ZrSi (group-3 materials), where "*x*" denotes the number of Pt ALD cycles administered on the materials. In this study, only 3 cycles of ALD was used to deposit Pt nanoparticles mainly because to keep its loading below 0.5 wt%.

2.3. Materials characterization

High-angle (5-90°) powder X-ray diffraction (XRD) was carried out on the materials using a PANanalytical X'Pert multipurpose X-ray diffractometer with Cu Kα radiation ($\lambda_1 = 1.5406$ Å, $\lambda_2 = 1.5444$ Å with $K\alpha_2/K\alpha_1 = 0.5$) and a scan rate of $2\theta = 0.7°$/min to determine the crystallinity and phase composition of the materials. Zero diffraction silicon plates (SIL'TRONIX) were used for the XRD measurement to eliminate any background noise from the XRD analysis. On a Micromeritics 3Flex Surface Characterization analyzer, N_2 physisorption experiments were carried out at −196 °C to assess the textural properties of the materials. Prior to each experiment, 0.1 g of the test sample was loaded in a BET tube and then degassed under vacuum at 250 °C for 12 h in a Micromeritics Smart VacPrep. Using the isotherm, the surface areas of the materials were determined by using the linearized Brunauer-Emmett-Teller (BET) model in the relative pressure range of $0.05 < P/P_0 < 0.35$, whereas non-local density functional theory (NLDFT) cylindrical geometry classical Harkins and Jura N_2-model was used to determine the pore volume, and pore size distribution (PSD). Moreover, transmission electron microscopy (TEM) was performed on each sample on a Zeiss Merlin Gemini field emission microscope (FE-SEM). X-ray photoelectron spectroscopy (XPS) spectra were collected on a Kratos Axis 165 photoelectron spectrometer with an aluminum X-ray source to quantify the surface elemental compositions and determine the surface elemental chemical states on the materials. The platinum weight percentages of the bulk materials were determined by inductively coupled plasma optical emission spectroscopy (ICP-OES) using a 2000D Perkin Elmer, and the samples were dissolved by a mixture of H_2SO_4 and HNO_3. Finally, ammonia (NH_3) temperature-programmed desorption (NH_3-TPD) experiments were performed in a flow reactor system to assess the surface acidity of the materials. For each experiment, 0.1 g of material was placed in a U-shaped quartz tube (8 mm I.D.) and degassed at 400 °C for 1 h under a He flow. After cooling to 80 °C under the same He flow, the loaded sample was exposed to a 5% NH_3/He flow for 30 min, and then to a He flow to remove physisorbed NH_3. Thereafter, the temperature was ramped from 80 to 800 °C at 10 °C/min for NH_3 desorption to take place under a He flow, and the desorbed amount being measured volumetrically using a mass spectrometer (MS, MKS Cirrus 2). When required, the flow rate used was set at 30 mL/min in the experiments.

2.4. *Equilibrium adsorption measurements*

Isotherm experiments were carried out on the materials to determine their equilibrium adsorption capacity and thus their economic feasibility for separation/purification purposes. In order to do this, volumetric measurements of the benzene vapor adsorption isotherms of the materials were carried out at 25 °C on the Micromeritics 3Flex Surface Characterization analyzer. Liquid benzene held at 25 °C and 1 atm was used to generate the vapor used for the measurements. The generated benzene vapor was thoroughly purified using the freeze–thaw purification method, by which the benzene liquid was purified at 77 K to remove any trapped gas impurities and then vaporized at 25 °C. The liquid benzene reservoir was immersed in a water bath kept at 25 °C throughout the duration of the experiment. For each experiment, 0.1 g of the test sample was loaded in a BET tube, degassed *in-situ* at 250 °C for 6 h under vacuum and then cooled to 25 °C, before being transferred to the Micromeritics 3Flex for the isotherm measurements.

2.5. *Dynamic adsorption experiments*

Adsorption breakthrough experiments at 25 °C and 1 atm were carried out in a stainless-steel column setup depicted in part (**a**) of Fig. 1 to assess the dynamic adsorption capacity of benzene vapor on the materials. The flow rates through the system were controlled by using the Brooks mass flow controllers (5800), while the temperature was controlled by a heating tape, K-type thermocouple, and an Omega benchtop controller. For each material, 0.2 g was packed into the column and then degassed at 200 °C for 1 h under a 40 mL/min Ar flow. The column was subsequently cooled to the adsorption temperature (25 °C) followed by temperature stabilization for about 30 min. Then, 100 mL/min benzene/Ar feed at 25 °C and 1 atm was flown to the inlet of the bed to allow adsorption to take place. The bed outlet concentration was monitored on-line by a mass spectrometer (MS, BELMass). The bed exit gas stream was sent to a trap before discharging to the atmosphere.

2.6. *Sequential adsorption and desorption/catalytic oxidation experiments*

For these experiments, adsorption was executed until the VOC concentration of the bed outlet reached 5% of the bed inlet concentration, $P_{out}/P_{in} \approx 0.05$ (i.e., 5% breakthrough or 95% instantaneous capture). This was done to avoid release of benzene beyond environmentally permissible limit in breakthrough, otherwise it leads to counter-intuitive endeavor. At this junction, the process set-up was switched from the adsorption mode (Fig. 1**a**) to the preheating/desorption-catalytic oxidation mode (Fig. 1**b**) to initiate catalytic oxidation. In between the 5% breakthrough adsorption and the catalytic oxidation was preheating step when the bed was heated externally in a furnace to required reaction temperature (200 °C), passing through the desorption temperature (100 °C) under a regenerative airflow of 20 mL/min. During the catalytic oxidation step, 20 mL/min regenerative airflow was continuously fed into the fixed bed. At the attainment of the reaction temperature, the

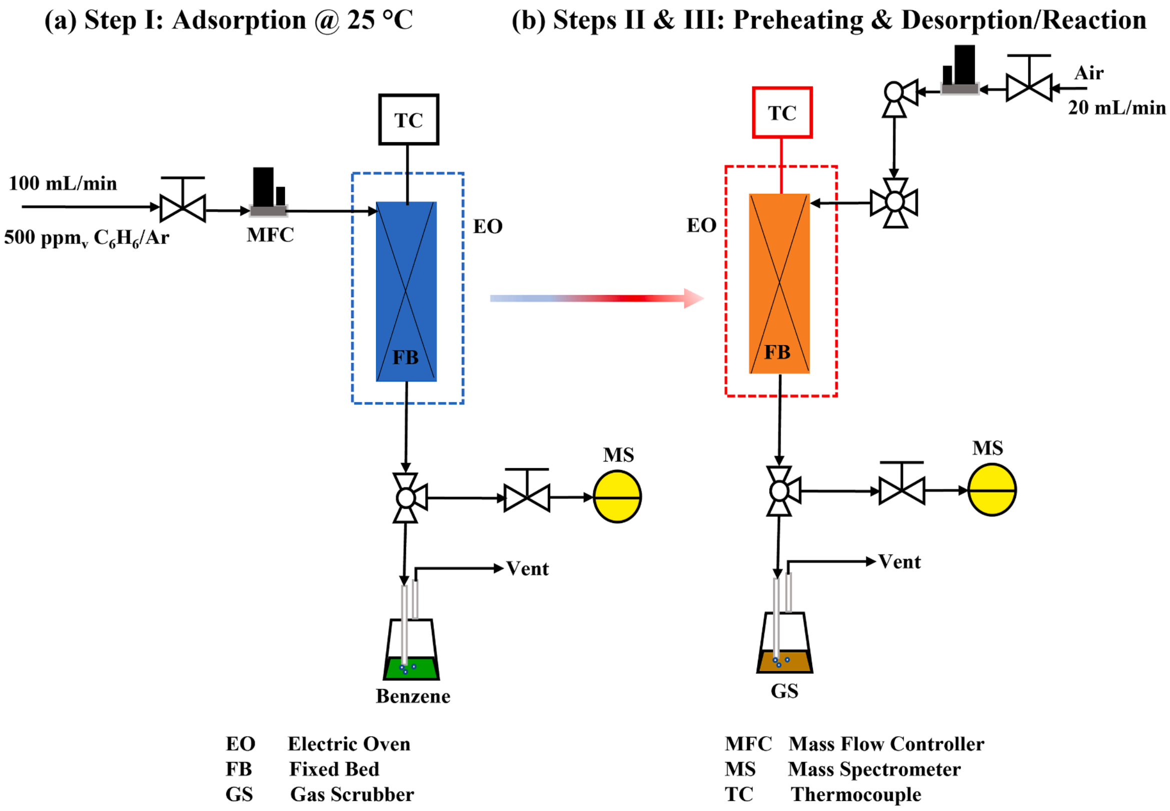

Fig. 1. Schematic of the single-column hybrid adsorption-catalytic oxidation experiment for (a) adsorption, and (b) preheating and desorption/reaction steps.

heat source was switched off to allow the process to run autothermally utilizing its exothermic heat of combustion. The bed outlet concentration during the sequential adsorption and catalytic oxidation process was collected on-line using the same MS (BELMass) used during the dynamic adsorption experiments. Carbon monoxide generation during the reaction was monitored by using Enerac 700 device.

3. Results and discussions

3.1. Materials Characterization

High-angle XRD patterns of the materials are shown in Fig. 2. Firstly, high-angle XRD was used here because it has been shown to contain a characteristic diffraction peak of silica, either synthetic or natural, around $2\theta = 22\text{-}23^\circ$ [21]. In all the materials, one peak situated around $2\theta = 22.5^\circ$, the characteristic diffraction peak of silica, has been indexed as plane (1 0 1) [22]. This peak is a bit broad, indicating that the materials are amorphous and thus lack any long-range orderly arrangement of atoms. Going to the patterns, we can see clearly that no significant difference is present either within any group or across groups of materials with the ZrO_2 or TiO_2 and/or Pt nanoparticles deposited on the base SiO_2 support. This suggests that the ZrO_2 or TiO_2 formed an ultrathin layer on the support or that it was amorphous and that the Pt nanoparticles were small and well dispersed thereon. Moreover, the non-appearance of Pt and/or TiO_2 or ZrO_2 peaks in the XRD patterns of all these materials may be due to the fact that the support had large surface area and that the Pt and TiO_2 or ZrO_2 particle sizes were small in the nanometer range as shall be confirmed later [23].

The TEM images of the materials 3Pt/Si, 3Pt/TiSi, and 3Pt/ZrSi are presented in Fig. 3 to reveal their interior surface morphology. TEM was carried out only for these three materials because each one of them came out to be the best material in its group as shall be seen later. In these images, dark spots represent Pt nanoparticles with sizes in the range of 2–3 nm. As evident from these images, the Pt nanoparticles were deposited uniformly throughout the surface for the three materials. Moreover, it also appears that the type of support does not significantly affect the size of deposited Pt nanoparticles, which may be due to lower Pt loading in these materials (i.e., only three ALD cycles were used). The uniformity in distribution of the Pt nanoparticles on the materials also appears to be similar in all the three samples. Given a very low thickness of TiO_2 or ZrO_2 films on the bare SiO_2, no significant changes in the morphology of these three samples can be observed. Moreover, TiO_2 and ZrO_2 deposition on the SiO_2 support in Fig. 3**b,c** seems to be present as few-nanometer thin layers, thus making it difficult for their identification by TEM [16]. On the basis of these results, it can be argued that Pt nanoparticles were uniformly dispersed into a previously-deposited thin layer of ZrO_2 or TiO_2 in the silica-based MMOs via ALD method.

Not only the distribution of Pt nanoparticles but also their electronic state is expected to be dependent on the nature of the metal oxide support. To assess any changes in the electronic state of these Pt nanoparticles in the three groups of materials and to confirm their composition, XPS analyses were performed. Changes in the binding strength of other elements such as O, Si, and Zr were also tracked. The profiles derived from the analyses are depicted in Fig. 4. It should be noted that these spectra have been adjusted with the adventurous C 1s peak at 284.5 eV due to observed charging effects during the XPS analyses. In Fig. 4**a,c,f**, Pt characteristic peaks were detected at 75.5 and 72.5 eV corresponding to Pt^{0+} $4f_{5/2}$ and $4f_{7/2}$, respectively. Comparison of the Ti spectra across three sets of samples revealed no significant changes in the electron state of Pt nanoparticles dispersed in different domains, indicating that the nature of metal oxide does not impact the electron state of Pt in these ALD-prepared samples. Expectedly, increases in Pt 4f peaks intensities and/or areas were observed as the number of the cycles of Pt ALD increased. Similarly, Si was detected across all the materials (Fig. 4**b,d,g**) at 103.5 eV, which corresponds to SiO_2 in the 2p atomic level. It is noteworthy that the intensity of Si 2p decreased with Pt loading similar to what was observed by Seo et al. [24]. In the group-2 materials, Ti was detected as Ti 2p located at 465 eV ($3d_{1/2}$) and 459 eV ($3d_{3/2}$) (Fig. 4**e**) corresponding with Ti^{4+}, while in the group-3 materials, a doublet of Zr 3d was detected, Zr $3d_{3/2}$ and Zr $3d_{5/2}$ at 185 and 182 eV, respectively (Fig. 4**h**) corresponding to Zr^{4+}. In Fig. 4**e,h**, there was not much difference in the intensity spans therein implying that the Ti and Zr amounts on the samples were fairly constant as expected in each group.

The materials surface elemental wt. % (via XPS) and bulk platinum wt. % (via ICP-OES) are shown in Table 1. First, it should be noted that the adventitious carbon C 1 s wt. % contribution has been deducted from the XPS data. As expected, Pt surface weight % loading increased linearly (0.13–0.33 wt% in group-1, 0.16–0.43 wt% in group-2 and 0.19–0.49 wt% in group-3) as the number of cycles of Pt administered on the materials increased from 1 to 2 to 3. The corresponding bulk wt. % via ICP-OES followed the same trend but with far higher values: 0.70–1.57, 1.39–5.01 and 2.38–5.37%, respectively. Expectedly, the Pt bulk weight % was higher than its surface weight % because of the high porosity (equivalently, high interior surface area) of the materials where most of the Pt nanoparticles are deposited deep in the pores of the materials. The surface amounts of Ti on the group-2 materials (2.39–2.60%) and Zr on the group-3 materials (1.36–1.50%) were very similar. Silicon surface wt. % is in the range of 31–34% while the oxygen wt. % is in the range of 65–67%, which shows Si/O atomic ratio to be ca. ½. This confirms that silicon exists in the form of SiO_2 in all the materials.

The N_2 physisorption (adsorption/desorption) isotherms and the pore size distributions (PSDs) of the materials are shown in Fig. 5. Within each group and across groups of materials, all the isotherms are similar in shape as was observed in the XRD patterns. Moreover, these materials have heterogeneous surface as three distinct stages of adsorption can be seen: first and monolayer adsorption, second and multilayer adsorption, and last and saturation adsorption. Across all the materials, the monolayer adsorption occurred in the range of $P/P_0 \leq 0.3$, the multilayer adsorption in the range of $0.3 \leq P/P_0 \leq 0.4$, while the saturation adsorption occurred in the range of $P/P_0 > 0.4$. The last and

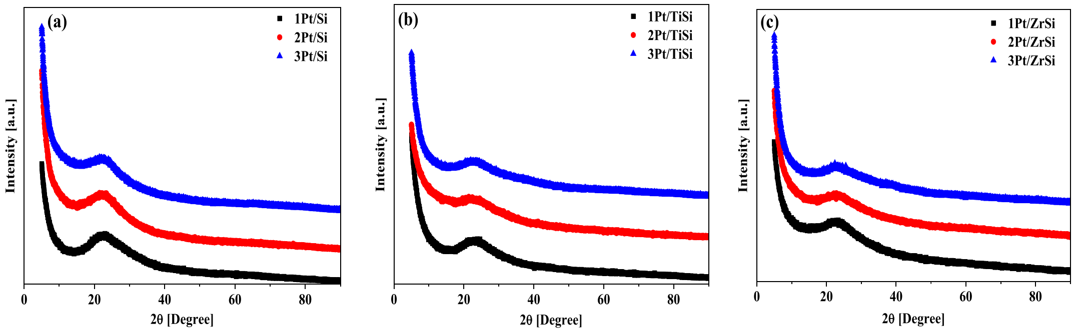

Fig. 2. High-angle XRD patterns of (a) *x*Pt/Si, (b) *x*Pt/TiSi and (c) *x*Pt/ZrSi.

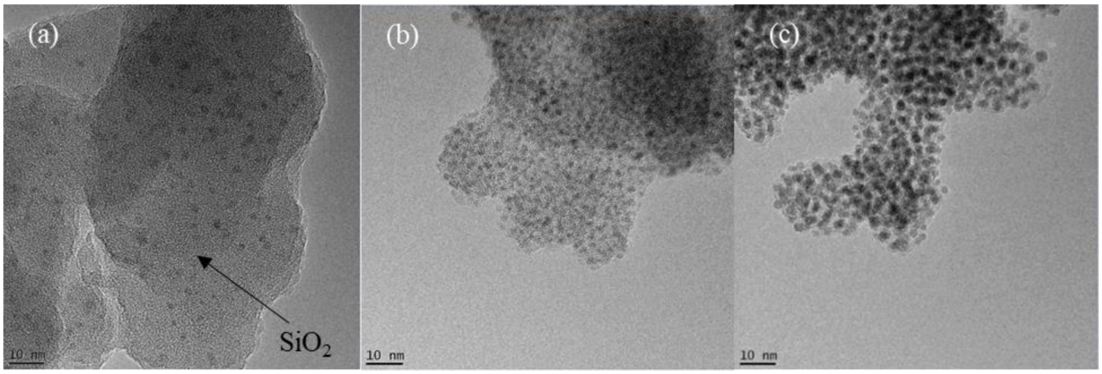

Fig. 3. TEM images of (a) 3Pt/Si, (b) 3Pt/TiSi, and (c) 3Pt/ZrSi. Black dots indicate Pt nanoparticles.

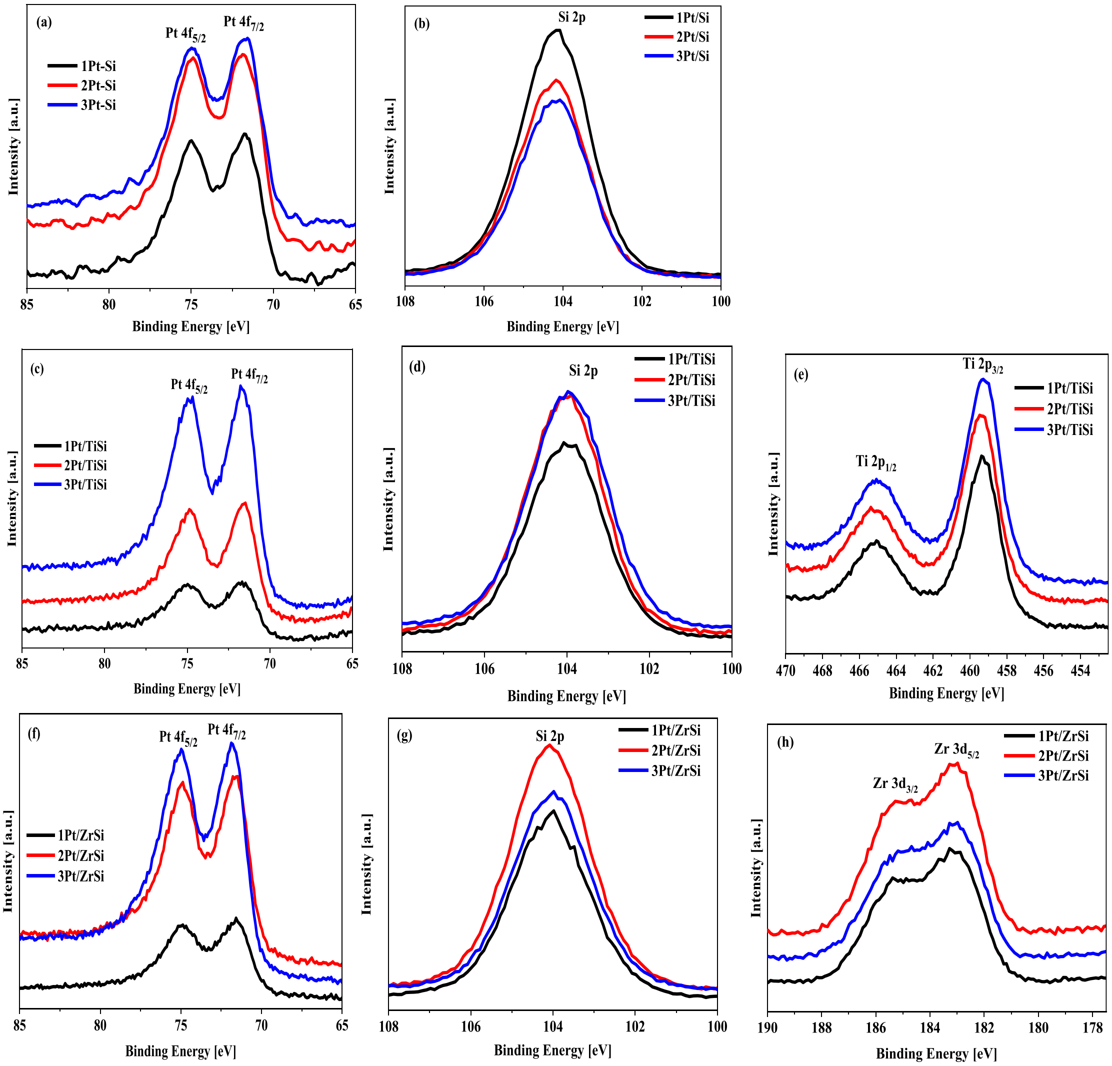

Fig. 4. XPS spectra of (a,b) *x*Pt/Si, (c-e) *x*Pt/TiSi and (f-h) *x*Pt/ZrSi.

saturation adsorption is associated with capillary condensation of N_2 taking place within the pores in the mesopore range [25]. The materials showed some level of sorption hysteresis which can be classified as the type H3, observed with aggregates of plate-like particles indicating the presence of slit-shaped pores in the materials [26]. The N_2 uptakes decrease in Fig. 5**a,b** but increase in Fig. 5**c** with Pt amount in accordance with the textural properties depicted in Table 1. Fig. 5**d-f** reveals that the PSDs maintain the same shape across all the materials and that the materials have bimodal mesopores with peaks centered about 3 and 5 nm, however with small amount of microporosity just below 2 nm pores. Finally, the N_2 physisorption and the PSD of the bare silica are higher than those of the composites, which was as expected.

The summary of the textural properties of the materials gathered from the N_2 physisorption results is shown in Table 2. Among the group-1 and group-2 materials, the surface area and pore volume decrease with Pt loading: *x*Pt/Si has 1276, 1206 and 1155 m^2/g, and 1.15, 1.06 and

Table 1
Materials surface elemental wt. % by XPS and bulk Pt wt. % by ICP-OES.

Sample	O	Si	Ti	Zr	XPS-Pt	ICP-OES Pt
	Atomic	Atomic	Atomic	Atomic	Atomic	Atomic
	[wt. %]	[wt. %]	[wt. %]	[wt. %]	[wt. %]	[wt. %]
1Pt/Si	66.61	33.27	–	–	0.13	0.70
2Pt/Si	66.60	33.23	–	–	0.18	1.26
3Pt/Si	66.11	33.56	–	–	0.33	1.57
1Pt/TiSi	66.12	31.24	2.49	–	0.16	1.39
2Pt/TiSi	65.73	31.67	2.39	–	0.21	2.96
3Pt/TiSi	65.93	31.04	2.60	–	0.43	5.01
1Pt/ZrSi	66.06	32.26	–	1.50	0.19	2.38
2Pt/ZrSi	66.15	32.17	–	1.36	0.32	4.17
3Pt/ZrSi	66.10	32.00	–	1.44	0.49	5.37

1.03 cm^3/g while *x*Pt/TiSi has 1140, 1066 and 832 m^2/g, and 0.94, 0.84 and 0.75 cm^3/g for × = 1, 2 and 3 respectively. The progressive loss in surface area and pore volume among the groups-1 and 2 materials is attributable to pore-blocking. In contrary, the group-3 (*x*Pt/ZrSi) materials depicted an increasing trend in surface area (962–1205 m^2/g) and pore volume (0.78–1.10 m^3/g) with Pt loading. For group-3 materials, there is a strong metal-support interaction which increases with metal loading due to high crystallinity of ZrO_2, which can also create intra-mesopores, whereas for group-2, Pt nanoparticles more likely deposit within the mesopores, thereby reducing the mesopore volume and surface area. Similar trend was observed in our first set of ALD DFMs with respect to Ni/ZrO_2 samples [19]. With respect to pore size, no significant changes to the pore size were observed within each group of materials, albeit a small decrease across group-1 to group-2 and group-3 was noticed at fixed Pt loading. The ALD ZrO_2 film in the group-3 materials may not be continuous, which can contribute to the increased surface area with Pt loading for this group [27]. Moreover, it should be noted that there were no differences in the near micropore sizes of these materials within each group probably because of the limited number of cycles of Pt deposited on the SiO_2 support, while the mesopores slightly decreased for the groups-1 and 2 but decreased for the group-3.

In this study, the type (weak, intermediate/medium and strong), density (volume of desorption: a measure of number of acid sites per desorption peak or in total), and strength (desorption temperature: a measure of desorption activation energy) of the acid sites present on the materials were determined through NH_3-TPD analysis, the profiles of which are shown in Fig. 8. The peak around 200 °C constitutes weak acid sites while the one above 400 °C constitutes medium to strong acid sites. Because the peak around 200 °C is common to all the materials, it could be attributed to Pt acid sites, which has been observed by other researchers [28,29]. Similarly, the peak above 400 °C could be attributed to SiO_2 acid sites. In Fig. 6**a** for the group-1 materials, the two types of

Table 2
Textural properties of the ALD materials and the bare silica.

Sample	BET Surface Area [m^2/g]	NLDFT Pore Volume [cm^3 STP/g]			NLDFT Pore Diameter [nm]
		Micropore	Mesopore	Total	
Bare Silica	1376	0.19	0.98	1.17	3.0, 5.2
1Pt/Si	1276	0.19	0.96	1.15	2.9, 5.1
2Pt/Si	1206	0.19	0.87	1.06	2.9, 5.1
3Pt/Si	1155	0.19	0.84	1.03	2.9, 5.1
1Pt/TiSi	1140	0.18	0.76	0.94	2.7, 5.0
2Pt/TiSi	1066	0.18	0.66	0.84	2.7, 5.0
3Pt/TiSi	832	0.18	0.57	0.75	2.7, 5.0
1Pt/ZrSi	962	0.17	0.61	0.78	2.7, 5.4
2Pt/ZrSi	1108	0.17	0.83	1.00	2.7, 5.4
3Pt/ZrSi	1205	0.17	0.93	1.10	2.7, 5.4

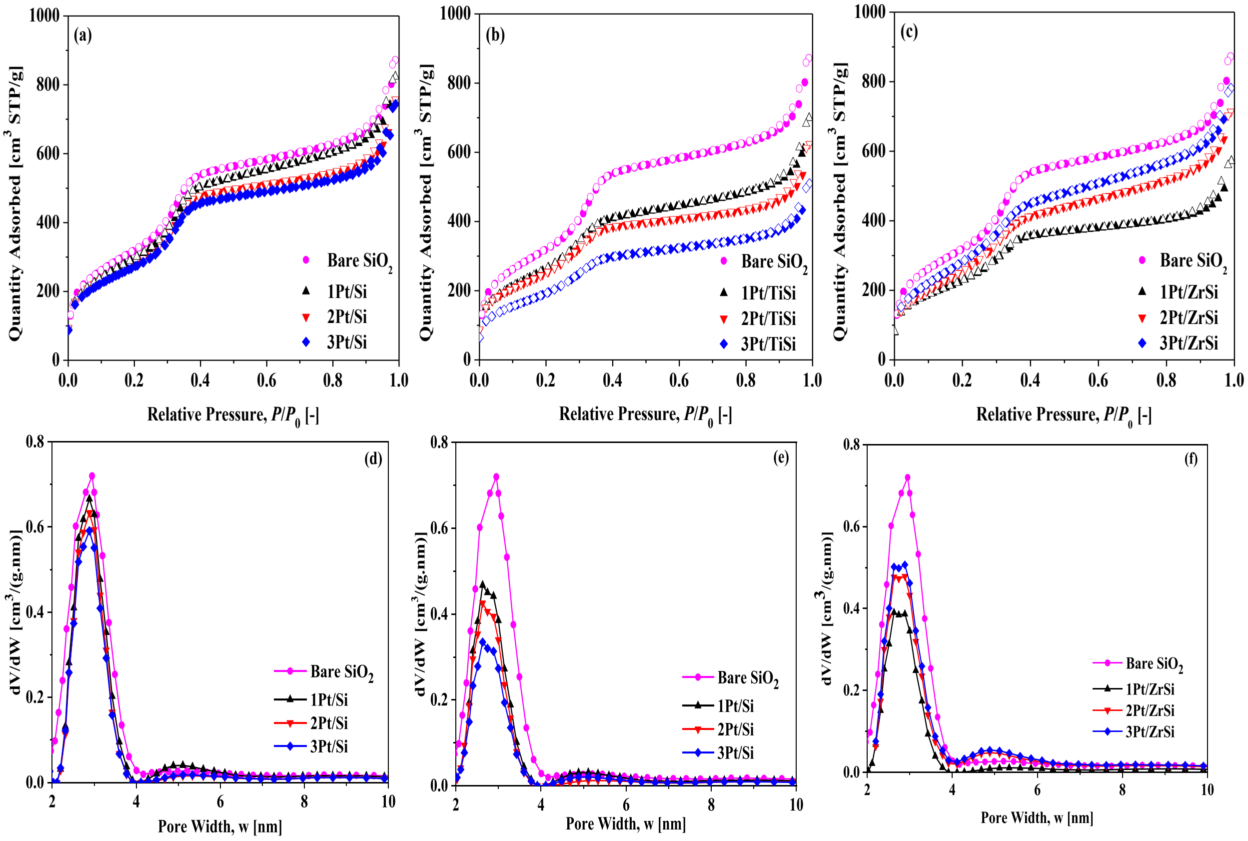

Fig. 5. (a-c) N_2 physisorption isotherms and (d-f) PSD profiles of *x*Pt/Si, *x*Pt/TiSi and *x*Pt/ZrSi.

acid sites mentioned above are present, with peak maxima at 183 and 558 °C, respectively. Clearly, as the Pt loading increased, the intensity and the area of the strong acid sites peak decreased with corresponding increase in those of the weak acid sites. In depth analysis revealed that a shift in the peak maxima values of NH_3-TPD profiles of the group-2 materials are shown in Fig. 6**b**. While 1Pt/TiSi clearly showed two distinct peaks, the other two materials of higher Pt loading showed just one peak (for Pt), the intensity of the other peak for SiO_2 was very small so that the peak could not be clearly observed. Fig. 6**c** shows the NH_3-TPD profiles of the group-3 materials. The Pt acid sites peak (around 200 °C) is clearly present, large and broad while the SiO_2 acid sites formed a shoulder around 450–800 °C. Going across the groups at a fixed Pt loading, we could see that the desorption peak maxima temperatures of all these materials were located at 183 and 558 °C, 180 and 547 °C, and 175 and 535 °C (for *x*Pt/Si); 164, 558 and 458 °C, 180, 547 and 698 °C, and 175, 535 and 741 °C (for *x*Pt/TiSi); and 183, 558 and 653 °C, 180, 547 and 698 °C, and 175, 535 and 741 °C (for *x*Pt/ZrSi) for $x = 1$–3 respectively. The total acid sites concentration and acid sites density of the materials are shown in Table 3. Clearly, the acid sites concentration increased with Pt loading, 0.0104–0.0168 mmol NH_3/g in group-1, 0.0518–0.2761 mmol NH_3/g in the group-2, and 0.2327–0.3024 mmol NH_3/g in group-3 same way the acid sites density increased. It is clear that when the Pt loading increased from cycle 1 to cycle 3, the NH_3 desorption peak increased correspondingly while the silica peak decreased. It is also clear that the higher the Pt content (up till 0.5 wt%), the higher the catalytic activity. It was conclusive that the presence of TiO_2 or ZrO_2 as part of the support increased the surface acidity of the bare SiO_2 and thus enhanced the material performance [30,31].

Table 3
Material dynamic adsorption data obtained from breakthrough profiles.

Sample	Pt Loading	Pt Acid Sites Concentration	Pt Acid Sites Density#
	[wt. %]	[mmol NH_3/g]	[mmol NH_3/m^2]
1Pt/Si	0.13	0.0104	8.1505×10^{-6}
2Pt/Si	0.18	0.0163	1.3516×10^{-5}
3Pt/Si	0.33	0.0168	1.4546×10^{-5}
1Pt/TiSi	0.16	0.0518	4.5439×10^{-5}
2Pt/TiSi	0.21	0.2466	2.3133×10^{-4}
3Pt/TiSi	0.43	0.2761	2.3185×10^{-4}
1Pt/ZrSi	0.19	0.2327	2.4188×10^{-4}
2Pt/ZrSi	0.32	0.2770	2.5000×10^{-4}
3Pt/ZrSi	0.49	0.3024	2.5096×10^{-4}

Acid Sites Density = Acid Sites Concentration/BET Surface Area.

3.2. Benzene adsorption isotherms

The benzene vapor adsorption isotherms are presented in Fig. 7. The insets therein are the isotherms in the range $0 \le P/P_0 \le 0.025$, around the dynamic adsorption VOC inlet partial pressure ($P/P_0 \approx 0.02$). In this low-pressure region, the adsorption capacity was more dependent on surface active sites than to surface area. Here, the adsorption capacity followed the order group-1 (0.69, 0.67 and 0.65 mmol/g) < group-2 (0.95, 0.91, and 0.80 mmol/g) ≈ group-3 (0.84, 0.88, and 0.97 mmol/g) at $P/P_0 \approx 0.02$ because of the more hydroxyl active sites created by TiO_2 or ZrO_2 [10]. However, as P/P_0 increased, the adsorption capacity followed the order group-1 > group-2 > group-3. For instance, at $P/P_0 \approx 0.7$, 1Pt/Si, 2Pt/Si, 3Pt/Si, 1Pt/TiSi, 2Pt/TiSi, 3Pt/TiSi, 1Pt/ZrSi, 2Pt/ZrSi, and 3Pt/ZrSi exhibited uptakes of 8.95, 8.35, 7.75, 8.05, 7.41, 6.45, 6.27, 6.79, and 7.35 mmol/g, respectively. For the groups-1 and 2 DFMs, equilibrium adsorption uptake decreased gradually with Pt loading, but increased in group-3. The trend observed herein is more dependent on the mesopore pore volume (due to higher adsorbate–adsorbate interactions at higher pressures) than the surface functionality by TiO_2 or ZrO_2. Across the entire relative pressure range, it is clear that all the materials depicted the same isotherm shape, typical of type IV isotherm according to the IUPAC classification [26]. Similar to the patterns observed in the N_2 physisorption experiments, the isotherms in Fig. 7 clearly display three consecutive stages of adsorption, namely monolayer adsorption, multilayer adsorption, and capillary condensation in the range of $0 \le P/P_0 \le 0.15$, $0.15 \le P/P_0 \le 0.25$, and $0.25 \le P/P_0 \le 1.00$, respectively. Moreover, it should be noted that the small and gradual change in equilibrium adsorption capacity observed within each group of materials especially at low pressure corresponds with the small difference in the number of cycles (1–3) of Pt deposited on these materials [32]. Similarly, it is worth to mention that these experiments could not be run till $P/P_0 \approx 1$ due to condensation formation at high pressure. In general, comparing the vapor isotherm of the bare silica to those of the composites revealed a gradual decrease in benzene uptake as similarly observed in the N_2 physisorption measurements.

3.3. Benzene dynamic adsorption experiments

Fig. 8 shows the results of the benzene dynamic adsorption experiments carried out on the materials, the blank run which helped in understanding the hydrodynamics of the empty column was also included. In the groups-1 and 2 materials, breakthrough characteristic times (5, 50 and 95% breakthroughs) decreased progressively with increasing Pt loading. However, only slight increases were observed in these characteristic times for the group-3 materials. In general, pore size, volume and size distribution, surface area, polarity/charge, roughness and functional groups, bed porosity and size, and inlet conditions (e.g., temperature, pressure/concentration and flow rate) are the major determinants of these times [33,34]. Because the dynamic adsorption experiments were all carried out under similar bed design variables and same operating conditions, then it is logical that material properties are the determinants of trends observed here. Moreover, it should be noted that the characteristic times were all in accordance with the trends observed in equilibrium adsorption uptakes at $P/P_0 \approx 0.02$ within each

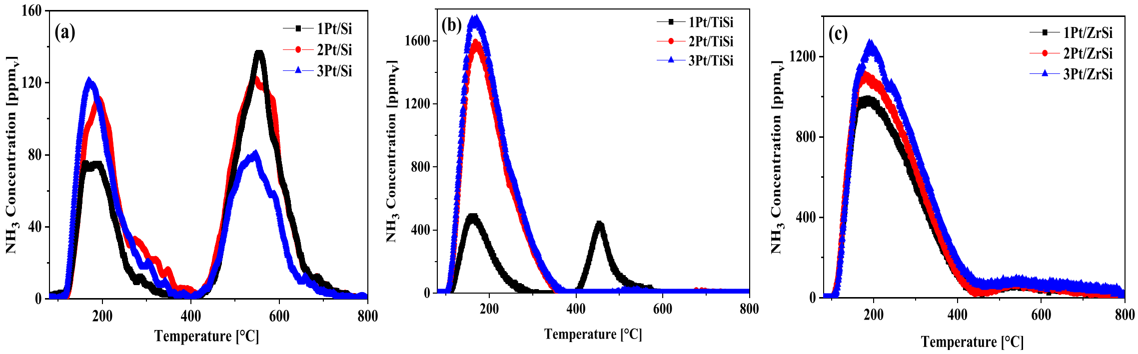

Fig. 6. NH_3-TPD profiles of (a) *x*Pt/Si, (b) *x*Pt/TiSi, and (c) *x*Pt/ZrSi from 80 to 800 °C.

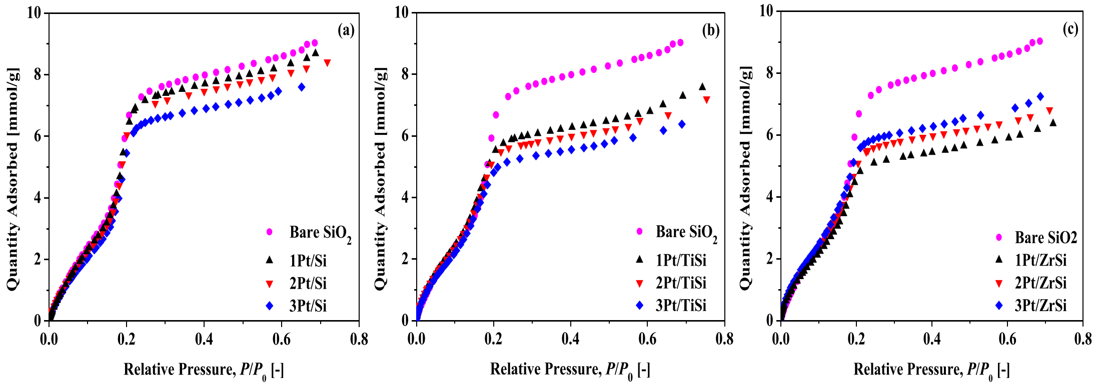

Fig. 7. Benzene vapor adsorption isotherms of (a) *x*Pt/Si, (b) *x*Pt/TiSi, and (c) *x*Pt/ZrSi.

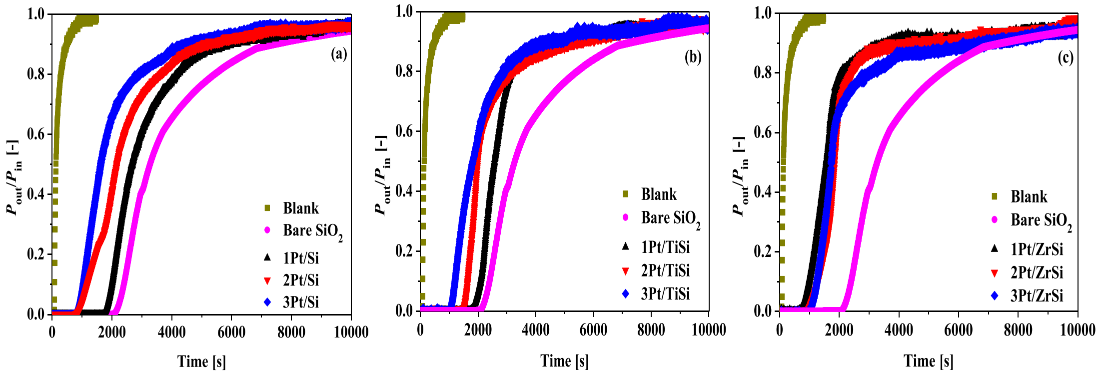

Fig. 8. Benzene vapor breakthrough profiles of (a) *x*Pt/Si, (b) *x*Pt/TiSi, and (c) *x*Pt/ZrSi.

group. Furthermore, it should also be noted that the adsorption characteristic times of the bare silica are higher than those of the composites because of decrease in surface area.

Key parameters from the breakthrough profiles depicted in Fig. 8 are summarized in Table 4. The equilibrium adsorption capacities of the materials at $P/P_0 \approx 0.02$ (equivalent to 500 ppm$_v$ at the bed inlet condition) were also included for comparison. With increasing Pt loading, the characteristic times $t_{0.05}$, $t_{0.5}$ and $t_{0.95}$ decreased linearly in the range of 1823–1050, 2454–1883 and 3085–2716 s in group-1, 1893–1297, 2766–1747 and 3639–2196 s for group-2 but increased in the range of 798–1028, 1523–1880 and 2248–2677 s in group-3. Similar trends were also observed in the values of $q_{d,0.05}$, $q_{d,0.5}$ and $q_{d,0.95}$. As expected, $q_{d,0.95}$ was lower than q_{eq}. Mokhatab et al. [35] showed that dynamic adsorption capacity ($q_{d,0.95}$) discrepancy from equilibrium adsorption capacity (qe_q) is usually about 30–50%, although the range in this work was 10–50% and the group-3 materials had the largest discrepancy. This discrepancy is usually due to flow effects, such as axial dispersion and/or mixing which suggests that there was higher flow dispersion and/or mixing in the group-3 materials, compared to the other two.

Table 4
Dynamic adsorption data obtained from breakthrough profiles.

Sample	$t_{0.05}$ [s]	$t_{0.5}$ [s]	$t_{0.95}$ [s]	$q_{d,0.05}$ [mmol/g]	$q_{d,0.5}$ [mmol/g]	$q_{d,0.95}$ [mmol/g]	q_{eq} @ $P/P_0 \approx 0.02$ [mmol/g]
Bare SiO$_2$	1930	2545	3215	0.35	0.51	0.64	0.95
1Pt/Si	1823	2454	3085	0.31	0.46	0.61	0.67
2Pt/Si	1472	2221	2971	0.25	0.33	0.40	0.64
3Pt/Si	1050	1883	2716	0.21	0.29	0.37	0.61
1Pt/TiSi	1893	2766	3639	0.32	0.42	0.52	0.87
2Pt/TiSi	1501	1948	2394	0.25	0.38	0.50	0.85
3Pt/TiSi	1297	1747	2196	0.18	0.32	0.46	0.76
1Pt/ZrSi	798	1523	2248	0.13	0.26	0.38	0.81
2Pt/ZrSi	1054	1712	2370	0.17	0.29	0.40	0.85
3Pt/ZrSi	1082	1880	2677	0.19	0.32	0.45	0.92

3.4. Sequential adsorption and desorption/catalytic oxidation performances

The results of the sequential adsorption and desorption/catalytic oxidation experiments performed on the DFMs are shown in Fig. 9. Because O_2 and N_2 were in excess in the system during the catalytic oxidation process, only the profiles of C_6H_6, CO_2, and H_2O are included in Fig. 9. It is noticeable that the transition from 5% breakthrough adsorption to desorption/catalytic oxidation started with initial roll-ups above $P_{out}/P_{in} \approx 0.05$. The overall inter/intraparticle holdup concentration of C_6H_6 at the attainment of 5% breakthrough adsorption, as well as the difference between the amount desorbed and the quantity oxidized, was responsible for these initial roll-ups. Because the inter/intraparticle concentration of C_6H_6 at the end of the 5% breakthrough adsorption had been completely pushed out of the bed or otherwise reacted, while the rate of desorption was still greater than the rate of oxidation, C_6H_6 concentration began to decrease shortly after the roll-ups had climaxed, as shown in Fig. 9. The C_6H_6 detection at this moment was due to higher desorption rate over catalytic oxidation rate. Complete oxidation of desorbed benzene was however accomplished

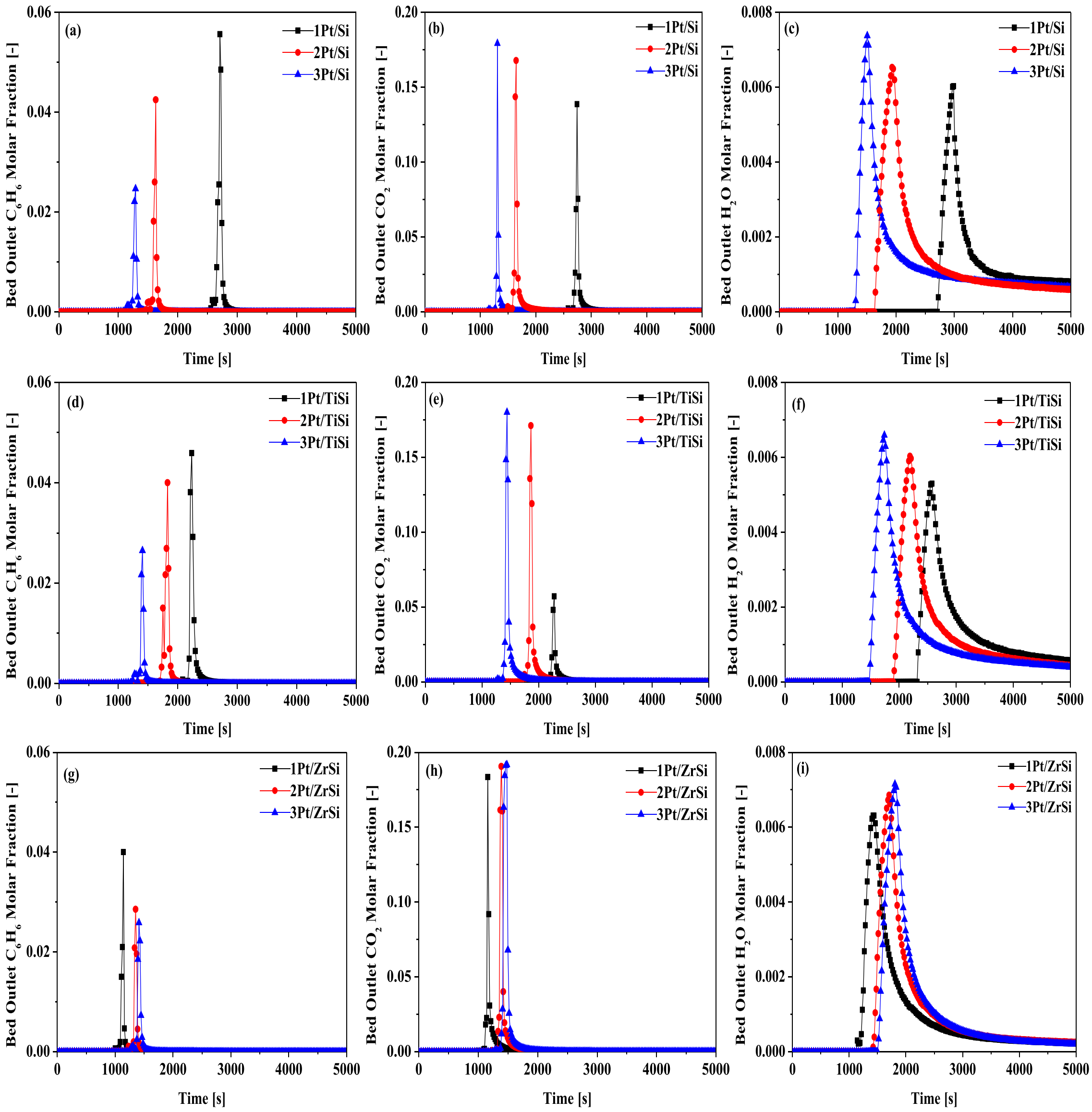

Fig. 9. Sequential adsorption and desorption/catalytic oxidation profiles of (a) 1Pt/Si, (b) 2Pt/Si, (c) 3Pt/Si, (d) 1Pt/TiSi, (e) 2Pt/TiSi, (f) 3Pt/TiSi, (g) 1Pt/ZrSi, (h) 2Pt/ZrSi, and (i) 3Pt/ZrSi.

approximately 15–20 min after the roll-ups climax, as shown in the profiles. As shown in Fig. 9**a,d,g**, C_6H_6 thermal runaway, i.e., desorbed but unreacted C_6H_6 decreased with Pt loading within each group. Similarly within any group, CO_2 and H_2O formation increased with Pt loading as shown in Fig. 9**b,c,e,f,h,i.** When going across the groups at a fixed Pt loading, C_6H_6 thermal runaway slightly decreased from *x*Pt/Si to *x*Pt/TiSi to *x*Pt/ZrSi [36], revealing that performance increased from *x*Pt/Si to *x*Pt/TiSi to *x*Pt/ZrSi. Similarly, within each group, performance increased with Pt loading based on the C_6H_6 thermal runaway amounts. The trends observed herein were all in accordance with the acid sites densities of these materials (Table 3).

Table 5

Oxidation performance variables (Overall *in-situ* conversion and TOF).

Sample	Overall *in-situ* Conversion (%)	Reaction TOF ($mmol_{C6H6}/mol_{Pt}/s$)
1Pt/Si	19.9	0.59
2Pt/Si	29.6	0.88
3Pt/Si	38.8	1.15
1Pt/TiSi	27.9	0.83
2Pt/TiSi	30.5	0.91
3Pt/TiSi	40.3	1.21
1Pt/ZrSi	97.1	10.6
2Pt/ZrSi	98.1	12.5
3Pt/ZrSi	99.6	17.1

Table 5 shows the summary of the process key performance indicators (benzene overall *in-situ* conversion and turnover frequency (TOF) on the DFMs). Within group-1, C_6H_6 overall conversion increased lineally with Pt loading: 19.9, 29.6, and 38.8% with corresponding TOF values of 0.57, 0.88, and 1.15 $mmolC_6H_6/mol_{Pt}/s$. A similar trend was also observed within groups-2 and 3 with values 27.9, 30.5 and 40.3%, and 97.1, 98.1, and 99.6%, respectively and corresponding values of 0.83, 0.91 and 1.21 $mmolC_6H_6/mol_{Pt}/s$ and 10.6, 12.5 and 17.1 $mmolC_6H_6/mol_{Pt}/s$. That the group-3 materials performed far better than the other two groups' was due to their high acid sites densities: a measure of the proximity of the Pt acid sites on the supports and also due to relatively lower dynamic adsorption loading [37]. The higher dual-functional capability of the Pt/ZrSi materials compared with Pt/TiSi materials could be attributed to their higher pore diameter, facilitating easy transfer of oxidant molecules to the catalytic active sites [38]. Comparison of the Pt/ZrSi materials with other bifunctional materials that have been reported in the literature, e.g., Ni/ZrSi materials for the same purpose revealed that these materials perform better for sequential adsorption and oxidation of benzene, a situation that is attributed to the higher catalytic activity of platinum relative to transition metal-based catalysts [19,37].

In summary, silica-supported and titania- or zirconia-promoted silica-supported Pt nanoparticles catalysts were investigated as adsorbent-catalyst DFMs for the abatement of dilute stream of benzene. Benzene equilibrium adsorption revealed type IV isotherm in all materials. Moreover, equilibrium uptake decreased with Pt loading among the groups-1 and 2 materials (xPt/SiO_2 and xPt/TiO_2-SiO_2, respectively), but increased among the group-2 materials (xPt/ZrO_2-SiO_2). Similarly, the benzene dynamic adsorption revealed a large uptake capacity up to about 7.5 mmol/g and fast adsorption kinetics. Successive adsorption and desorption/catalytic oxidation performed on the materials revealed that xPt/ZrO_2-SiO_2 completely outperformed the other two groups of materials for destruction of benzene. Results further revealed that the total conversion of benzene linearly increased with Pt loading: 97.1, 98.1, and 99.6% for xPt/ZrO_2-SiO_2 with $x = 2.4$, 4.2, and 5.4 wt%, respectively. Moreover, for all the materials investigated here, a higher H_2O yield was observed compared to that of CO_2. Overall, the findings of this investigation highlight the potential of novel ALD-prepared xPt/ZrSi as efficient DFMs for application in VOC abatement processes.

Declaration of Competing Interest

The authors declare that they have no known competing financial interests or personal relationships that could have appeared to influence the work reported in this paper.

Acknowledgments

The authors thank the National Science Foundation (NSF CBET-1802049) for financially supporting this project.

References

[1] C. Liaud, N.T. Nguyen, R. Nasreddine, S. Le Calvé, Experimental Performances Study of a Transportable GC-PID and Two Thermo-Desorption Based Methods Coupled to FID and MS Detection to Assess BTEX Exposure at Sub-Ppb Level in Air, Talanta 127 (2014) 33–42.

[2] T. Gelles, A. Krishnamurthy, B. Adebayo, A. Rownaghi, F. Rezaei, Abatement of Gaseous Volatile Organic Compounds: A Material Perspective, Catal. Today 350 (2020) 3–18.

[3] A. Krishnamurthy, B. Adebayo, T. Gelles, A. Rownaghi, F. Rezaei, Abatement of Gaseous Volatile Organic Compounds: A Process Perspective, Catal. Today 350 (2020) 100–119.

[4] E. Kullavanijaya, D.L. Trimm, N.W. Cant, Adsocat: Adsorption/Catalytic Combustion for VOC and Odour Control, Stud. Surf. Sci. Catal. 130 (2000) 569–574.

[5] E. Kullavanijaya, N.W. Cant, D.L. Trimm, The Treatment of Binary VOC Mixtures by Adsorption and Oxidation Using Activated Carbon and a Palladium Catalyst, J. Chem. Technol. Biotechnol. 77 (4) (2002) 473–480.

[6] K. Nikolajsen, L. Kiwi-Minsker, A. Renken, Structured Fixed-Bed Adsorber Based on Zeolite/Sintered Metal Fibre for Low Concentration VOC Removal, Chem. Eng. Res. Des. 84 (7) (2006) 562–568.

[7] Y. Wang, D. Yang, S. Li, M. Chen, L. Guo, J. Zhou, Ru/Hierarchical HZSM-5 Zeolite as Efficient Bi-Functional Adsorbent/Catalyst for Bulky Aromatic VOCs Elimination, Microporous Mesoporous Mater. 258 (2018) 17–25.

[8] M.A. Kolade, A. Kogelbauer, E. Alpay, Adsorptive Reactor Technology for VOC Abatement, Chem. Eng. Sci. 64 (6) (2009) 1167–1177.

[9] L. Yanyan, T.A. Kurniawan, M. Zhu, T. Ouyang, R. Avtar, M.H. Dzarfan Othman, B. T. Mohammad, A.B. Albadarin, Removal of Acetaminophen from Synthetic Wastewater in a Fixed-Bed Column Adsorption Using Low-Cost Coconut Shell Waste Pretreated with NaOH, HNO_3, Ozone, and/or Chitosan, J. Environ. Manage. 226 (2018) 365–376.

[10] B.O. Adebayo, S. Lawson, A.A. Rownaghi, F. Rezaei, Analysis of Equilibrium and Dynamic Adsorption of Benzene Vapor over Unimodal and Bimodal Silica-Based Mixed-Metal Oxides, Chem. Eng. J. 396 (2020), 125273.

[11] E. Barea, Montoro, J.A.R. Navarro, Toxic Gas Removal–Metal–Organic Frameworks for the Capture and Degradation of Toxic Gases and Vapours, Chem. Soc. Rev. 43 (2014) 5419–5430.

[12] M. Bahri, F. Haghighat, H. Kazemian, S. Rohani, A Comparative Study on Metal Organic Frameworks for Indoor Environment Application : Adsorption Evaluation, Chem. Eng. J. 313 (2017) 711–723.

[13] L.F. Liotta, Catalytic Oxidation of Volatile Organic Compounds on Supported Noble Metals, Appl. Catal. B Environ. 100 (3) (2010) 403–412.

[14] H. Huang, Y. Xu, Q. Feng, D.Y.C. Leung, Low Temperature Catalytic Oxidation of Volatile Organic Compounds: A Review, Catal. Sci. Technol. 5 (5) (2015) 2649–2669.

[15] H. Kim, T. Kim, H. Koh, S. Lee, B. Min, Complete Benzene Oxidation over Pt-Pd Bimetal Catalyst Supported on γ-Alumina: Influence of Pt-Pd Ratio on the Catalytic Activity, Elsevier, 2005, pp. 125–131.

[16] E.J. Park, J.H. Lee, K.D. Kim, D.H. Kim, M.G. Jeong, Y.D. Kim, Toluene Oxidation Catalyzed by NiO/SiO_2 and NiO/TiO_2/SiO_2: Towards Development of Humidity-Resistant Catalysts, Catal. Today 260 (2016) 100–106.

[17] H.J. Lee, H.O. Seo, D.W. Kim, K.D. Kim, Y. Luo, D.C. Lim, H. Ju, J.W. Kim, J. Lee, Y. D. Kim, A High-Performing Nanostructured TiO_2 Filter for Volatile Organic Compounds Using Atomic Layer Deposition, Chem. Commun. 47 (19) (2011) 5605–5607.

[18] Ho, S. M.; S.A, V.; Ahmed, G.; Vidya, N. S. A Review of Nanostructured Thin Films for Gas Sensing and Corrosion Protection. *Mediterr. J. Chem.* **2018**, *7* (6), 433–451.

[19] B.O. Adebayo, K. Newport, H. Yu, A.A. Rownaghi, X. Liang, F. Rezaei, Atomic Layer Deposited Ni/ZrO_2-SiO_2 for Combined Capture and Oxidation of VOCs, ACS Appl. Mater. Interfaces 12 (35) (2020) 39318–39334.

[20] X. Liang, L.F. Hakim, G.D. Zhan, J.A. McCormick, S.M. George, A.W. Weimer, J. A. Spencer, K.J. Buechler, J. Blackson, C.J. Wood, J.R. Dorgan, Novel Processing to Produce Polymer/Ceramic Nanocomposites by Atomic Layer Deposition, J. Am. Ceram. Soc. 90 (1) (2007) 57–63.

[21] E. Soto-Cantu, R. Cueto, J. Koch, P.S. Russo, Synthesis and Rapid Characterization of Amine-Functionalized Silica, Langmuir 28 (13) (2012) 5562–5569.

[22] Munasir, Triwikantoro, M. Zainuri, Darminto, Synthesis of SiO_2 Nanopowders Containing Quartz and Cristobalite Phases from Silica Sands, Mater. Sci. Pol. 33 (2015) 47–55.

[23] C.V. Miguel, R. Trujillano, V. Rives, M.A. Vicente, A.F.P. Ferreira, A.E. Rodrigues, A. Mendes, L.M. Madeira, High Temperature CO_2 Sorption with Gallium-Substituted and Promoted Hydrotalcites, Sep. Purif. Technol. 127 (2014) 202–211.

[24] H.O. Seo, D.H. Kim, K.-D. Kim, E.J. Park, C.W. Sim, Y.D. Kim, Adsorption and Desorption of Toluene on Nanoporous TiO_2/SiO_2 Prepared by Atomic Layer Deposition (ALD): Influence of TiO_2 Thin Film Thickness and Humidity, Adsorption 19 (6) (2013) 1181–1187.

[25] D. Ortiz de Zárate, A. Gómez-Moratalla, C. Guillem, A. Beltrán, J. Latorre, D. Beltrán, P. Amorós, High-Zirconium-Content Nano-Sized Bimodal Mesoporous Silicas. *Wiley Online*, Library 2006 (13) (2006) 2572–2581.

[26] K.S.W. Sing, Reporting Physisorption Data for Gas/Solid Systems with Special Reference to the Determination of Surface Area and Porosity (Provisional), Pure Appl. Chem. 54 (11) (1982) 2201–2218.

[27] D. Goma, J.J. Delgado, L. Lefferts, J. Faria, J.J. Calvino, M.Á. Cauqui, Catalytic Performance of Ni/CeO_2/X-ZrO_2 (X = Ca, Y) Catalysts in the Aqueous-Phase Reforming of Methanol, Nanomaterials 9 (11) (2019) 1582.

[28] M.-Y. Kim, J.-S. Choi, T.J. Toops, E.-S. Jeong, S.-W. Han, V. Schwartz, J. Chen, Coating SiO_2 Support with TiO_2 or ZrO_2 and Effects on Structure and CO Oxidation Performance of Pt Catalysts, Catalysts 3 (2013) 88–103.

[29] D. García-Pérez, M. Consuelo Alvarez-Galvan, J.M. Campos-Martin, J.L.G. Fierro, Influence of the Reduction Temperature and the Nature of the Support on the Performance of Zirconia and Alumina-Supported Pt Catalysts for *n*-Dodecane Hydroisomerization, Catalysts 11 (1) (2021) 88.

[30] B. Tyagi, Kalpesh, B. Sidhpuria, Basha, S. Raksh, V. Jasra, Effect of Zr/Si Molar Ratio and Sulfation on Structural and Catalytic Properties of ZrO_2-SiO_2 Mixed Oxides, J. Porous Mater. 17 (2010) 699–709.

[31] A. Al-Mamoori, A.A. Rownaghi, F. Rezaei, Combined Capture and Utilization of CO_2 for Syngas Production over Dual-Function Materials, ACS Sustain. Chem. Eng. 6 (10) (2018) 13551–13561.

[32] H.O. Seo, C.W. Sim, K.-D. Kim, Y.D. Kim, D.C. Lim, Nanoporous TiO2/SiO2 Prepared by Atomic Layer Deposition as Adsorbents of Methylene Blue in Aqueous Solutions, Chem. Eng. J. 183 (2012) 381–386.

[33] J.E. Szulejko, K.H. Kim, J. Parise, Seeking the Most Powerful and Practical Real-World Sorbents for Gaseous Benzene as a Representative Volatile Organic Compound Based on Performance Metrics, Sep. Purif. Technol. 212 (2019) 980–985.

[34] B.A. Adebayo, F. Rezaei, Modeling of Temperature Swing Adsorption-Oxidation of Volatile Organic Compounds, Chem. Eng. Sci. 250 (2022), 117356.

[35] S. Mokhatab, W. Poe, J. Mak, Handbook of Natural Gas Transmission and Processing - Google Books, 2006.

[36] D. Ortiz De Zarate, A. Gomez-Moratalla, C. Guillem, A. Beltran, J. Latorre, D. Beltran, P. Amoros, High-Zirconium-Content Nano-Sized Bimodal Mesoporous Silicas, Eur. J. Inorg. Chem. 13 (2006) 2572–2581.

[37] A. Urbutis, S. Kitrys, Dual Function Adsorbent-Catalyst CuO-CeO_2/NaX for Temperature Swing Oxidation of Benzene, Toluene and Xylene, Cent. Eur. J. Chem. 12 (4) (2014) 492–501.

[38] S. Huang, C. Zhang, H. He, In Situ Adsorption-Catalysis System for the Removal of o-Xylene over an Activated Carbon Supported Pd Catalyst, J. Environ. Sci. 21 (7) (2009) 985–990.